Determinants of endocytic membrane geometry, stability, and scission

Takuma Kishimoto, Yidi Sun, Christopher Buser, Jian Liu[1], Alphée Michelot, and David G. Drubin[2]

Department of Molecular and Cell Biology, University of California, Berkeley, CA 94720-3202

Edited by Pietro De Camilli, Yale University and Howard Hughes Medical Institute, New Haven, CT, and approved September 21, 2011 (received for review August 16, 2011)

During endocytic vesicle formation, distinct subdomains along the membrane invagination are specified by different proteins, which bend the membrane and drive scission. Bin-Amphiphysin-Rvs (BAR) and Fer-CIP4 homology-BAR (F-BAR) proteins can induce membrane curvature and have been suggested to facilitate membrane invagination and scission. Two F-BAR proteins, Syp1 and Bzz1, are found at budding yeast endocytic sites. Syp1 arrives early but departs from the endocytic site before formation of deep membrane invaginations and scission. Using genetic, spatiotemporal, and ultrastructural analyses, we demonstrate that Bzz1, the heterodimeric BAR domain protein Rvs161/167, actin polymerization, and the lipid phosphatase Sjl2 cooperate, each through a distinct mechanism, to induce membrane scission in yeast. Additionally, actin assembly and Rvs161/167 cooperate to drive formation of deep invaginations. Finally, we find that Bzz1, acting at the invagination base, stabilizes endocytic sites and functions with Rvs161/167, localized along the tubule, to achieve proper endocytic membrane geometry necessary for efficient scission. Together, our results reveal that dynamic interplay between a lipid phosphatase, actin assembly, and membrane-sculpting proteins leads to proper membrane shaping, tubule stabilization, and scission.

endocytosis | cytoskeleton | electron microscopy

Endocytosis involves a succession of plasma membrane remodeling steps (1). First, the membrane is locally deformed to generate a shallow invagination, which is subsequently extended into a deep invagination. Next, the invagination neck constricts until a vesicle is pinched off. These dynamic membrane-remodeling steps are achieved through temporally and spatially regulated protein-lipid and protein-protein interactions. Although numerous studies have documented activities of individual endocytic proteins in vitro and in vivo, the actual biological functions of these proteins can only be understood when the function of each protein is perturbed in vivo during endocytosis and the effects are analyzed dynamically and ultrastructurally.

Real-time imaging and genetic studies in yeast suggested that the proteins and lipids involved in endocytic vesicle formation can be grouped into a coat module, a Bin-Amphiphysin-Rvs (BAR) protein module, an actin module, a phosphatidylinositol (4,5)-bisphosphate [PI(4,5)P_2] module, and a synaptojanin [PI(4,5)P_2 phosphatase] module (2–5). Importantly, although a wealth of information about biochemical activities, dynamics, and spatial organization of the key molecular players in endocytosis has accumulated, a coherent view of how the various proteins mediate membrane remodeling steps is only now beginning to emerge.

In addition to coat proteins, several other proteins help to shape endocytic membranes and pinch off vesicles. For example, from yeast to mammals, banana-shaped dimeric BAR and F-BAR proteins bind preferentially to curved membranes and induce membrane curvature. The BAR domain protein amphiphysin functions with dynamin and actin during membrane tubulation and scission in mammalian cells (6, 7), and it preferentially binds to negatively charged lipids, such as phosphatidyl serine and PI (4,5)P_2 (8). Because F-BAR domain proteins generally bind to membranes of lower curvature relative to BAR domain proteins (9–12), it has been suggested that they might associate with the base of the invagination (13). In budding yeast, two F-BAR proteins, Syp1 (14) and Bzz1, and the heterodimeric BAR protein Rvs161/167 are recruited to endocytic sites with distinct timing, suggesting distinct functions in membrane remodeling, and evidence supports the conclusion that Bzz1 and Rvs161/167 localize at the invagination base and along the tubule, respectively (4, 15).

Actin assembly is integrally linked to endocytic membrane invagination in yeast and in mammalian cells (5, 7, 15–22). Whether the actin cytoskeleton has specific functions in membrane scission is not clear. Because disruption of actin assembly in yeast blocks membrane invagination (5), new strategies are needed to test for actin function in membrane scission.

The lipid PI(4,5)P_2 is also a key endocytic regulator (2, 23–26). A complete understanding of endocytosis will therefore require analysis of how the lipid phosphatase synaptojanin, actin, BAR, and F-BAR proteins contribute to plasma membrane remodeling and scission.

Results and Discussion

Reduced Scission Efficiency in Mutants of Rvs161/167 BAR Proteins Provides an Opportunity to Identify Additional Scission Factors Genetically and Chemically. We developed a genetic strategy to identify factors that function in endocytic vesicle scission. The endocytic coat/adaptor protein Sla1 was previously established as a marker for endocytic internalization in vivo (5, 27). In WT cells, Sla1-red fluorescent protein (RFP) first assembles at the cell cortex and then moves toward the cell interior during membrane invagination (Fig. 1 *A* and *B*). As we showed previously, deletion of *RVS161* or *RVS167*, which encode the subunits of a heterodimeric BAR protein, results in a unique phenotype: Sla1-GFP moves off the cell surface but fails to be released and retracts back to the cell surface (5) (Fig. 1 *A* and *B*). We proposed that this phenotype represents failure of membrane scission. Consistent with this interpretation, the Rvs proteins arrive at the endocytic site just before scission (5, 28).

To verify that Sla1 retraction in *rvs167*Δ mutants represents scission failure, we examined the dynamics of a fluorescently labeled endocytic cargo, Alexa Fluor-488 C_5-α-factor (A488 α-factor) in *rvs167*Δ cells. When Sla1-RFP retracted back to the cell surface in *rvs167*Δ mutant cells, A488 α-factor patches also retracted to the cell surface (100% of Sla1 retraction events, $n = 15$) (Fig. 1*C*, *Right* and Movie S1). A kymograph shows cor-

---

Author contributions: T.K., Y.S., C.B., and A.M. designed research; T.K., Y.S., C.B., and A.M. performed research; T.K., Y.S., C.B., J.L., A.M., and D.G.D. analyzed data; and T.K., Y.S., C.B., J.L., and D.G.D. wrote the paper.

The authors declare no conflict of interest.

This article is a PNAS Direct Submission.

[1] Present address: Computational Biology Laboratory, National Heart, Lung, and Blood Institute, National Institutes of Health, Department of Health and Human Services, Bethesda, MD 20892.

[2] To whom correspondence should be addressed. E-mail: drubin@berkeley.edu.

See Author Summary on page 17865.

This article contains supporting information online at www.pnas.org/lookup/suppl/doi:10.1073/pnas.1113413108/-/DCSupplemental.

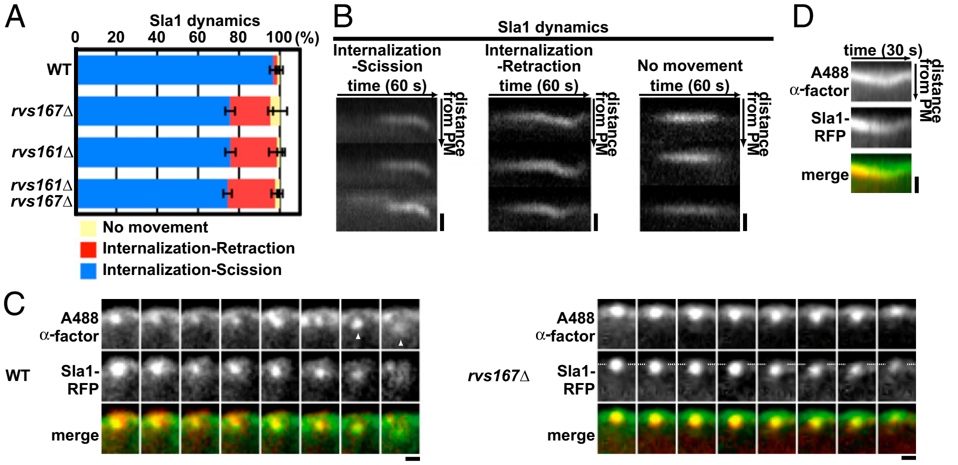

Fig. 1. Endocytic vesicle scission assay. (*A*) Sla1-GFP dynamics in *rvs167*Δ and *rvs161*Δ mutants. Blue, red, and yellow bars represent the percentages of patches that were internalized followed by scission, that were internalized followed by retraction to the plasma membrane (PM), and that did not internalize, respectively. (*B*) Kymographs of single patches from movies of Sla1-GFP in an *rvs167*Δ mutant. Three patterns described in *A* are displayed. Each panel shows three individual patches. (Scale bars: 400 nm.) (*C*) Colocalization of fluorescent α-factor with internalizing (WT cells) and retracting (*rvs167*Δ mutant cells) Sla1-RFP patches. The time series shows the position of endocytic patches from movie frames (1 frame per second). Images from 3-s intervals are shown. (*Left*) White arrowheads represent a released endocytic vesicle in WT cells. (*Right*) Dashed lines represent the position of Sla1-RFP origin parallel to the PM. (Scale bars: 200 nm.) (*D*) Kymograph representations of fluorescent α-factor and Sla1-RFP for a single patch in an *rvs167*Δ mutant from a two-color movie (1 frame per second). (Scale bar: 200 nm.)

respondence between retracting α-factor and Sla1-RFP in an *rvs167*Δ mutant (Fig. 1*D*). These results validate Sla1-RFP retraction behavior as a reporter of membrane scission failure.

Interestingly, the Sla1-GFP retraction phenotype is not fully penetrant in *rvs161*Δ or *rvs167*Δ cells, as we reported previously (5). Both *rvs161*Δ and *rvs167*Δ single mutants (19.7% ± 1.2 and 21.5% ± 3.9, respectively) and *rvs161*Δ *rvs167*Δ double mutants (23.2% ± 1.8) only displayed a partial scission defect (Fig. 1*A*). This partial penetrance suggests that proteins of other endocytic modules are also involved in endocytic vesicle scission. However, our previous analysis of Sla1-GFP dynamics in over 60 endocytic mutants revealed that the retraction phenotype is unique to *rvs* mutants (5). Although the yeast dynamin Vps1 was reported to be present at endocytic sites and to contribute to efficient scission (29), we failed to find evidence for its recruitment to endocytic sites or a strong contribution to scission. Only 3.93% of Abp1-marked endocytic patches showed coincident Vps1 localization (Table S1), and the *vps1*Δ mutant did not enhance the retraction incidence of an *rvs167*Δ mutant in our analysis (Fig. S1*A*). Although a consensus has not yet been reached on whether Vps1 plays a direct role in endocytosis, there is general agreement that, in contrast to the situation in mammalian cells, Vps1 does not play an obligate role in endocytic vesicle scission.

We used a genetic enhancer strategy to identify factors important for scission. We reasoned that diminution of the function of a protein involved in scission in combination with an *rvs* mutant should specifically enhance the scission defect. The function of various endocytic proteins was perturbed in the *rvs* null background, and we tested for enhancement of the scission defect by quantifying Sla1-GFP retraction events.

Robust Actin Polymerization Is Required for Endocytic Membrane Scission in the Absence of the Rvs Proteins. Actin polymerization is required for formation of endocytic membrane invaginations in yeast, making assessment of actin's contribution to scission difficult. Previous studies found that high concentrations of Latrunculin-A (Lat-A), a drug that sequesters actin monomers, block invagination (27), whereas low concentrations slow actin assembly at endocytic sites but still allow invagination formation (30). We tested whether levels of Lat-A that have undetectable or barely detectable effects in WT cells would increase Sla1-GFP retraction in an *rvs167*Δ background. As shown in Fig. 2*A*, actin patches can assemble in 16 μM Lat-A in WT cells or in 4 μM Lat-A in *rvs167*Δ mutant cells. In WT cells, Sla1 patch internalization decreased in a dose-dependent manner in the presence of Lat-A, but retraction events did not increase (Fig. 2*B* and Movie S2). Strikingly, patch internalization in *rvs167*Δ mutant cells was much more sensitive to Lat-A, which indicates that actin assembly and BAR proteins cooperate to drive endocytic invagination formation. Moreover, Sla1 retraction was markedly increased by addition of Lat-A at concentrations of only 0.5 μM (24% retraction) to 2 μM (55% retraction) (Fig. 2*C* and Movie S2), which had essentially no effect on patches in WT cells (Fig. 2*B*). These results reveal synergistic contributions of actin polymerization and BAR protein assembly to both membrane invagination and vesicle scission.

To explore how different regulators of actin polymerization contribute to membrane scission, we examined endocytic scission efficiency in mutants of various actin nucleation-promoting factors (NPFs) in an *rvs167*Δ background. Different NPFs likely nucleate actin filaments for different functions at endocytic sites (15, 31). In budding yeast, the Arp2/3 complex is activated by several NPFs, including Pan1, type I myosins Myo3/5, and the Wiskott–Aldrich syndrome protein (WASP)-related Las17, through carboxyl-terminal Arp2/3 binding (CA) domains and the WASP CA (WCA) domain in Las17 (15, 31–34). The NPF activities of both Las17 and Myo5 are significantly higher than that of Pan1 in vitro, and Las17 and Myo5 NPF activities play particularly crucial roles in vivo (15). Las17 arrives at endocytic sites earlier than Myo5, and these two proteins primarily initiate assembly and promote internalization, respectively. Importantly, deletion of the CA domain of either Las17 or Myo5 severely reduced its NPF activity in vitro but had only modest effects on endocytic internalization in vivo, suggesting that in the absence of one NPF, the other can partially substitute (15, 35, 36) (Fig. 2*D* and Movie S3). We combined *rvs167*Δ mutants with mutants of the Arp2/3 activation domains of Las17 (*las17-WCA*Δ), Pan1 (*pan1-CA*Δ), and Myo5 (*myo5-CA*Δ), respectively (Fig. 2*D*). Strikingly, scission failure increased in *rvs167*Δ *las17-WCA*Δ mutants (69%) or *rvs167*Δ *myo5-CA*Δ mutants (49%) but not in *rvs167*Δ *pan1-CA*Δ mutants (18%), compared with scission in *rvs167*Δ mutants (19.7%). These results establish that robust actin nucleation triggered by Las17 and Myo5 contributes to mem-

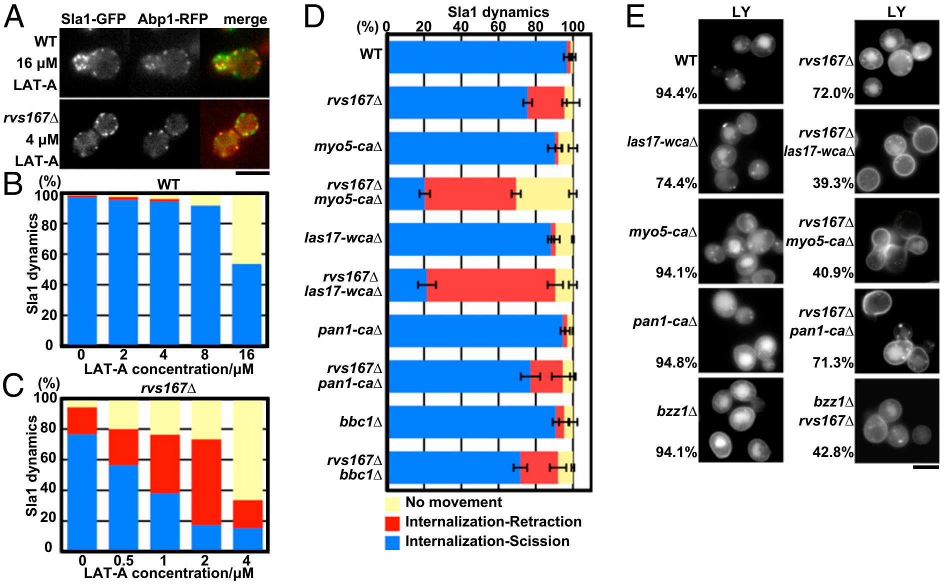

Fig. 2. Importance of actin assembly and Myo5, Las17, and Pan1 NPF activity for membrane scission. (*A*) Single frames from live-cell movies showing Sla1-GFP localization at a Lat-A concentration that allows actin assembly at endocytic sites. Sla1-GFP dynamics in WT (*B*) and *rvs167*Δ mutant (*C*) cells treated with Lat-A. Results shown are representative of three independent experiments. (*D*) Sla1-GFP dynamics in strains carrying *rvs167*Δ combined with site-directed mutations in genes encoding NPF proteins, specifically eliminating their Arp2/3-activating activity. Data shown are the mean ± SD. Three independent experiments were performed. (*E*) Fluorescence microscopy analysis of LY endocytic uptake. Cells were incubated with LY for 2 h at 25 °C. Means are the fractions of the cells displaying LY accumulation in the vacuole. (Scale bars: *A* and *E*, 5 μm.)

brane scission. The lack of enhancement of the *rvs167*Δ scission defect by the *pan1-CA*Δ, the *vps1*Δ, or an *end3*Δ mutant (Fig. S1) demonstrates the specificity of the observed effects.

We next performed a fluid-phase endocytosis assay on the same set of mutants, quantifying the percentage of cells scoring positive for vacuole fluorescence. Both *pan1-CA*Δ and *myo5-CA*Δ displayed normal vacuole staining with Lucifer Yellow (LY) (94% of cells scored normal for uptake, *n* = 124), whereas the *las17-WCA*Δ exhibited a modest LY uptake defect (74.7% of cells scored normal for uptake, *n* = 186) (Fig. 2*E*). However, LY uptake was strongly reduced in the *rvs167*Δ *las17-WCA*Δ double-mutant cells (29% of cells scored normal for uptake, *n* = 105) and in the *rvs167*Δ *myo5-CA*Δ double-mutant cells (35%) but not in the *rvs167*Δ *pan1-CA*Δ mutant cells (71%). Thus, the LY uptake results correspond well with the increased Sla1 retraction rates, which our α-factor assay (Fig. 1 *C* and *D*) established as a measure of scission failure rate. These results support the conclusion that robust actin nucleation and BAR protein assembly function together to drive both the membrane invagination and the scission steps of the endocytic pathway.

We also asked whether increased NPF activity can compensate for the *rvs167*Δ scission defect in vivo by eliminating Bbc1. Bbc1 inhibits Las17's NPF activity in vitro (15, 37, 38), and its absence causes overactivation of actin nucleation in vivo (5, 37). As shown in Fig. 2*D*, *BBC1* deletion did not improve the scission efficiency in *rvs167*Δ mutants. These results suggest that actin polymerization and BAR proteins make mechanistically distinct contributions to membrane scission.

How actin polymerization contributes to membrane scission is now an important question. Filament assembly might generate a pinching force that contributes directly to membrane scission. Indeed, actin polymerization can deform lipid vesicles in vitro (39) and contributes to endocytic membrane constriction in mammalian cells (7, 20, 40). Alternatively, actin filament association with membranes can influence the local lipid distribution (41), and might therefore contribute to lipid phase segregation (42). Such an effect might be augmented by actin-mediated pulling forces (41). A line tension at the phase boundary might drive scission (2, 43). Indeed, Römer et al. (44) implicated actin in membrane reorganization in Shiga toxin-induced endocytic membrane tubules, which they suggested, in turn, promoted scission. In vitro experiments (45–48) and theoretical models (43, 49, 50) suggest that the interfacial force generated at a lipid phase boundary could generate sufficient force to induce membrane scission.

Involvement of Invagination Tip-Associated Synaptojanin Sjl2 in Scission. Previously, by mutating two of the three budding yeast synaptojanins, we showed that hydrolysis of PI(4,5)P_2 phosphates is important for multiple endocytic steps, including vesicle scission (26), and we proposed that BAR proteins, which are recruited to endocytic sites at essentially the same time as synaptojanin, function cooperatively with synaptojanin to mediate scission (2). Because the *sjl1*Δ *sjl2*Δ double mutant used in our previous studies has a pronounced global deficit in PI(4,5)P_2 levels (51), it was important to test the specificity of synaptojanin's scission function via a less severe disruption of synaptojanin function. Thus, to explore the functional relationship between BAR proteins and synaptojanin, we both turned off and overexpressed *SJL2* in *rvs167*Δ cells. Sjl2 is the only yeast synaptojanin present specifically at endocytic sites, where it is recruited to invagination tips around the time of scission (26, 52). Loss of Sjl2 expression in *rvs167*Δ cells caused a pronounced synergistic decrease in scission efficiency, from 20% failure to 55% failure (Fig. 3*A* and Movie S4). Additionally, Sjl2 overexpression using the powerful pGal promoter reduced the frequency of the membrane scission defect in the *rvs167*Δ mutant from 20% to 8% (Fig. 3*B*). These studies suggest that hydrolysis of PI(4,5)P_2 phosphates has a specific role in endocytic vesicle scission. Sjl2 might promote scission by generating a lipid phase boundary (2), relaxing membrane tension on the tubule by triggering release of coat proteins attached to assembling actin filaments (53), or both.

F-BAR Protein Bzz1 Works with the BAR Protein Rvs161/167 to Promote Endocytic Vesicle Scission. Accumulating evidence suggests that BAR and F-BAR proteins, which share structural fea-

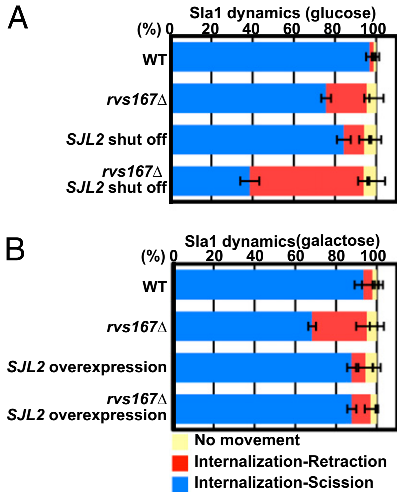

Fig. 3. Synaptojanin Sjl2 contributes to membrane scission. (*A*) Sla1-RFP dynamics in WT or *rvs167*Δ cells with or without P_{GAL1}-*GFP-SJL2* cultured in glucose-containing medium to turn off *SJL2* expression. Lack of GFP-Sjl2 expression was confirmed by fluorescence microscopy. (*B*) Effect of *GFP-SJL2* overexpression on Sla1-RFP dynamics in WT or *rvs167*Δ cells with or without P_{GAL1}-*GFP-SJL2*. Cells were cultured in galactose-containing medium to induce *GFP-SJL2* overexpression. Data shown are the mean ± SD.

tures and bind to curved membranes, may function as links between the actin polymerization apparatus and curved membranes (15, 54, 55). However, the precise biological functions of BAR and F-BAR proteins are still not clear. Budding yeast have only one BAR protein, Rvs161/167, but have five F-BAR proteins: Syp1, Bzz1, Hof1, and Rgd1/2. Syp1 and Bzz1 but not Hof1 and Rgd1/2 are found at endocytic sites. Syp1 may play a role in generating initial curvature, but this protein departs from endocytic sites before they become deeply invaginated (3, 14). In contrast, Bzz1 is recruited to endocytic sites at the onset of formation of the deeply invaginated membrane. Bzz1 is a syndapin-like protein, which has a predicted N-terminal F-BAR domain and two C-terminal Src homology 3 (SH3) domains (Fig. 4*A*). Bzz1 physically interacts with and activates Las17 and localizes to endocytic patches (15, 34, 37, 38). However, *BZZ1* deletion alone did not cause a readily detectable actin, endocytic, or growth phenotype (15).

To test whether Bzz1 has a role in membrane scission, we generated *bzz1*Δ *rvs167*Δ double mutants and quantified Sla1-GFP retraction events. Strikingly, the Sla1-GFP retraction frequency was markedly higher in *bzz1*Δ *rvs167*Δ cells (45%) than in *rvs167*Δ cells (21.5%) (Fig. 4*B* and Movie S5). Consistently, *bzz1*Δ *rvs167*Δ cells exhibited a significantly more severe LY uptake defect (42% of cells scored for normal uptake) than *rvs167*Δ cells (72%) (Fig. 2*E*). Correspondingly, *bzz1*Δ *rvs167*Δ cells grew very poorly, whereas *rvs167*Δ cells grew relatively normally at 25 °C (Fig. 4*C*), in agreement with published data (56). Combining mutants of the other three known F-BAR proteins, Syp1, Hof1, and Rgd1/2, with *rvs167*Δ had no effect on scission efficiency, consistent with the early arrival and departure of Syp1 and the absence of Hof1 and Rgd1/2 at endocytic sites. Together, these results identify Bzz1 as an F-BAR protein important for efficient endocytic vesicle scission.

In the first part of our study, we showed that robust actin nucleation activity is important for endocytic membrane scission. Also, we previously demonstrated that Bzz1 relieves Sla1 inhibition of Las17 NPF activity in vitro (15). Thus, one possibility was that Bzz1 affects membrane scission by regulating Las17 NPF activity. To test this possibility, we generated *bzz1*Δ *rvs167*Δ in the background of the *las17-WCA*Δ mutant, which has severely diminished Las17 NPF activity. Strikingly, more than 80% of Sla1-GFP patches displayed retraction movements in *bzz1*Δ *rvs167*Δ *las17-WCA*Δ triple mutants, which was more severe than in *las17-WCA*Δ *rvs167*Δ double mutants (69% of patches; $P = 0.011$) (Fig. 4*B*). This in vivo genetic analysis establishes that loss of Bzz1's interaction with Las17 is not the sole cause of the enhanced membrane scission defect observed in the *bzz1*Δ *rvs167*Δ mutant, a conclusion that is further supported by analysis of Sla1 retraction frequency in *bzz1*Δ *rvs167*Δ *bbc1*Δ mutants. Bbc1 inhibits Las17's NPF activity (5, 37). However, these triple mutants displayed similar Sla1-GFP retraction rates to the *rvs167*Δ *bzz1*Δ double mutant (46.6% of patches). Together, these results suggest that Bzz1 contributes to membrane scission via a mechanism independent of its actin assembly activity. Corresponding to the high incidence of Sla1-GFP retraction, *bzz1*Δ *rvs167*Δ *las17-WCA*Δ triple mutants displayed a more severe growth defect than *bzz1*Δ *rvs167*Δ or *rvs167*Δ *las17-WCA*Δ double mutants (Fig. 4*C*).

Although sequence homology (Fig. 4*A*) identifies a highly probable F-BAR domain in Bzz1, we performed a preliminary analysis of the protein's interaction with itself and lipids to support this identification. We expressed Bzz1-HA and Bzz1-Myc alleles in a diploid strain, finding that Bzz1-Myc coimmunoprecipitates with Bzz1-HA, whereas control Bzz1 without an HA or myc tag does not (Fig. 4*D*, *Lower*). These data indicate that Bzz1 associates with itself, similar to mammalian F-BAR proteins. Furthermore, as shown in Fig. 4*E*, Bzz1 bound to liposomes containing phosphatidylcholine (PC), phosphatidylethanolamine (PE), and 5% PI(4,5)P_2 but not to liposomes containing only PC and PE. We next purified recombinant Bzz1 in which a conserved positively charged residue in the presumed F-BAR domain was changed to glutamate (R37E) (Fig. 4*A*). This allele was modeled after the K33E mutant of the F-BAR protein FBP17, which causes a defect in membrane binding and tubulation activities (13). As shown in Fig. 4*E*, the analogous mutant of Bzz1 also caused a significant decrease in binding to PC/PE/PI(4,5)P_2 liposomes. These results indicate that an arginine residue conserved in F-BAR proteins is important for Bzz1 binding to PI(4,5)P_2-containing lipid bilayers.

To explore the function of the Bzz1 F-BAR domain in scission in living cells, we generated a *bzz1-R37E-GFP* mutant allele and first analyzed its localization. Real-time imaging demonstrated that Bzz1-R37E-GFP localized to cortical patches in a similar manner to the WT protein (Fig. 4*F*), consistent with the observation that Bzz1 is recruited to endocytic sites through its SH3 domain (38). The lifetime of Bzz1-R37E-GFP at patches is shorter relative to the WT protein (from 16 s to 12 s). The recruitment of the mutant protein to endocytic sites provided an opportunity to test the importance of the F-BAR domain for scission. Similar to a *bzz1*Δ mutant, the *bzz1-R37E* mutant did not show a pronounced retraction phenotype (Fig. 4*G* and Movie S5). However, when the *bzz1-R37E* mutant was combined with *rvs167*Δ, the Sla1-GFP retraction frequency increased to 41% (Fig. 4*G*), which is very similar to the frequency in the *rvs167*Δ *bzz1*Δ cells. These results establish that Bzz1 F-BAR domain function is important for membrane scission. Importantly, Bzz1 and Bzz1-R37E mutant proteins both released Sla1 inhibition of Las17's NPF activity to a similar level in vitro (Fig. S2), supporting the conclusion that the Bzz1 F-BAR domain affects membrane scission independent of Bzz1's effects on Las17 NPF activity.

Bzz1 F-BAR Protein Associates with the Base of the Endocytic Invagination. To investigate further how Bzz1 and Rvs167 cooperate to promote membrane scission, we examined Bzz1 and Rvs167 spatiodynamics simultaneously by two-color live-cell imaging. Rvs167-RFP assembly at the endocytic site is characterized by a rapid increase in fluorescence, followed by a rapid decrease at the time of scission (5, 28) (Fig. 5*A*). Simultaneous, two-color live-cell imaging confirmed that Bzz1 arrives at endocytic sites before Rvs167 and that Bzz1 persists at the plasma membrane,

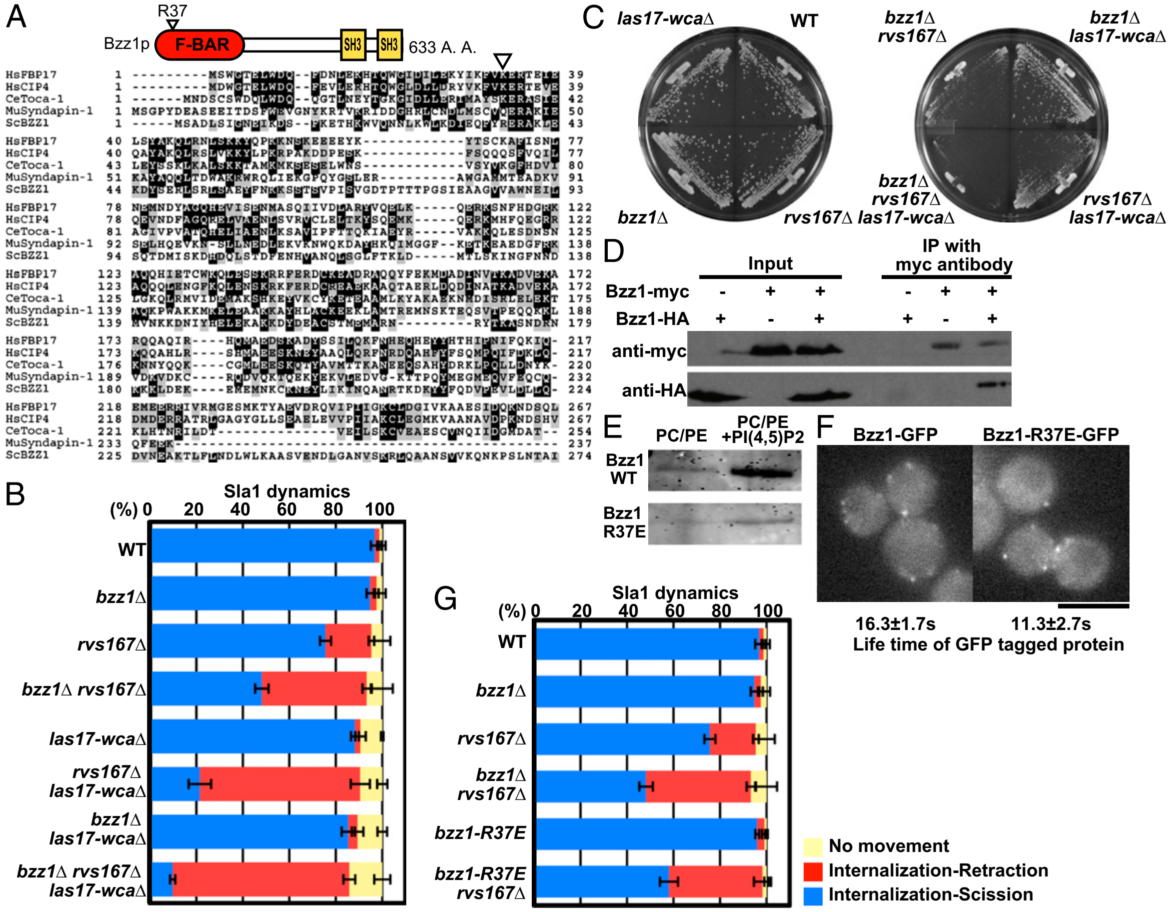

Fig. 4. F-BAR protein Bzz1 contributes to membrane scission synergistically with Rvs proteins and actin assembly. (*A*) Domain structure of Bzz1 and sequence alignment of F-BAR domains from different proteins. Black boxes indicate identical amino acids (A. A.). Gray boxes indicate similar A. A. The open inverted triangle (R37E) above the sequences indicates the mutated A. A. residue. (*B*) Sla1-GFP dynamics in a *bzz1Δ rvs167Δ las17-WCAΔ* triple mutant. Data shown are the mean ± SD. (*C*) Deletion of *BZZ1* exacerbates the growth defect of the *las17-WCAΔ rvs167Δ* double mutant. After streaking cells, YPD plates were incubated at 25 °C for 2 d. The results shown are representative of results for four independent clones for each genotype. (*D*) Coimmunoprecipitation (IP) of Bzz1-HA and Bzz1-Myc from extracts of heterozygous diploid cells. Immunoblot analyses using antibodies against Myc (*Upper*) and HA (*Lower*) are shown. The results presented are representative of three experiments. (*E*) Binding of Bzz1 and mutant Bzz1 to liposomes made from PC/PE mix with or without 5 mol% PI(4,5)P_2. (*F*) Fluorescence image of GFP-tagged Bzz1 and Bzz1 mutants. Means for the lifetime of Bzz1-GFP ± SD were calculated from at least 50 patches from 10 cells. (Scale bar: 5 μm.) (*G*) Sla1-GFP dynamics in the *bzz1* mutant combined with the *rvs167Δ* mutant. Data shown are the mean ± SD.

whereas Rvs167 moves into the cytoplasm (15) (Fig. 5 *A* and *B*). Consistently, live-cell imaging and immuno-EM previously revealed that Rvs167 localizes along the tubules of invaginated membranes (4, 5).

To verify that Bzz1 is at the base of endocytic invaginations, we quantitatively analyzed, frame by frame, the positions of Bzz1, Myo5, and Sla1 centroids in movies and calculated the distances between the mean centroid positions. Myo5 and Bzz1 have been suggested to interact physically and to function together at the base of endocytic invaginations (4, 5, 38). When 60 Bzz1 and Myo5 patches were examined in movies from 15 cells, the average closest and farthest distances separating their centroid positions were 20.6 ± 11.9 nm and 60.0 ± 21.6 nm, respectively, during the time when both proteins were present at endocytic sites. However, when 78 Bzz1 and Sla1 patches in 18 cells were examined, the average closest and farthest distances separating their centroid positions were 39.2 ± 27.1 nm and 155.4 ± 62.8 nm, respectively, during the time when both proteins were present at endocytic sites.

These results are consistent with the observation that in reconstituted endocytic patches, Bzz1 decorates the Las17-coated beads, whereas Rvs167 associates with actin tails (55). Thus, Bzz1 arrives first at the endocytic site and remains at the base of the invagination, whereas Rvs167 arrives subsequently and coats the tubule, suggesting unique roles for these two proteins in endocytic membrane remodeling.

Bzz1 F-BAR Protein Stabilizes Endocytic Invaginations. Previous studies revealed that deletion of *BBC1* increases the distance of Sla1 inward movement (5). As a result, Sla1 retraction movements can be observed more clearly in *rvs167Δ bbc1Δ* mutants (Fig. 5*C*, *Left* and Movie S6). Unexpectedly, in a *bzz1Δ rvs167Δ bbc1Δ* triple mutant, Sla1-GFP patches retracted toward a different position from their origin (Fig. 5*C*, *Right* and Movie S6). Tracking of individual retracting Sla1-GFP patches in *rvs167Δ bbc1Δ* and *bzz1Δ rvs167Δ bbc1Δ* mutants using a particle-tracking algorithm (27) further supported this surprising observation (Fig. 5*D*). As shown in Fig. 5*E*, on average, the centers of Sla1-GFP fluorescence ended 84 nm (*n* = 40 from 10 cells) from the original internalization position in *rvs167Δ bbc1Δ* mutants, and 178 nm (*n* = 50 from 14 cells) from the original internalization position in *bzz1Δ rvs167Δ bbc1Δ* mutants. Because centroids for endocytic sites in WT cells showed movements of ~70–80 nm, this range is likely a reflection of the limit of the precision with which the position of a fluorescence centroid could be determined. Importantly, in *bzz1-R37E rvs167Δ bbc1Δ* triple mutants, Sla1-GFP patches also retracted to a

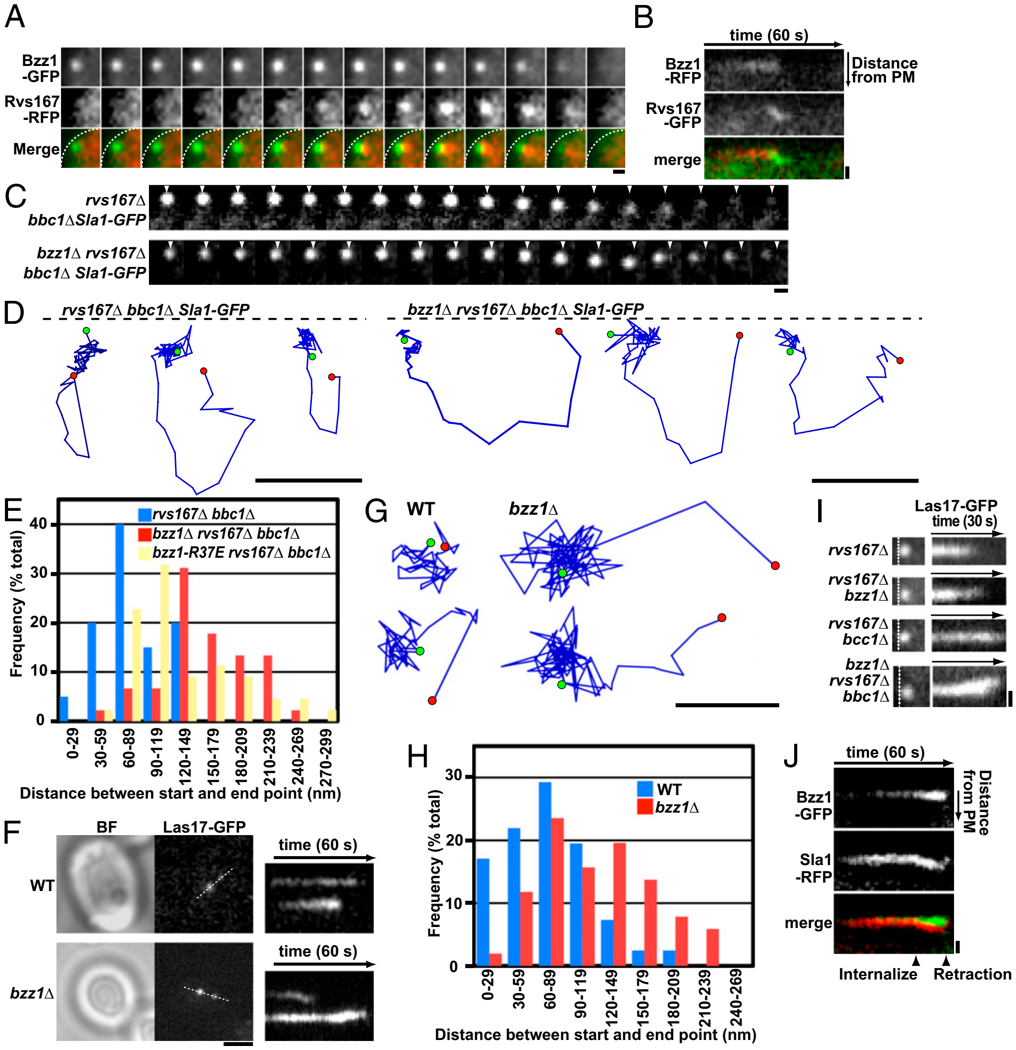

Fig. 5. Bzz1 associates with and stabilizes the base of endocytic membrane invaginations. (*A*) Dynamic localization of Rvs167-RFP relative to Bzz1-GFP in living cells. The time series shows the composition of individual patches from two-color movies (1 frame per second). White dashed lines in merged images represent the plasma membrane (PM). (Scale bar: 300 nm.) (*B*) Kymograph representation of Rvs167-GFP and Bzz1-RFP in a single patch from a two-color movie. Kymographs are oriented with the cell exterior at the top. (Scale bar: 400 nm.) (*C*) Displacement of Sla1-GFP from its starting position on retraction to the PM in *rvs167Δ bbc1Δ* and *bzz1Δ rvs167Δ bbc1Δ* mutants. The time series shows the position of individual patches from single-color movies (1 frame per second). Arrowheads represent starting positions. (Scale bar: 200 nm.) (*D*) Tracking of individual Sla1-GFP patches in *rvs167Δ bbc1Δ* and *bzz1Δ rvs167Δ bbc1Δ* mutants. The positions of the centers of patches were identified in each frame of a movie (1 frame per second) from the medial focal plane of a cell. Consecutive positions from the start (green) to the end (red) were connected by lines. Patch traces are oriented so that the cell surface is up (dashed line) and the cell interior is down. The time difference between each position along the track is 1 s. (Scale bars: 200 nm.) (*E*) Histogram shows the distribution of distances between the appearance and disappearance sites for retracting Sla1 patches in the *rvs167Δ bbc1Δ*, *bzz1Δ rvs167Δ bbc1Δ*, and *bzz1-R37E rvs167Δ bbc1Δ* mutants. (*F*) TIRF microscopy analysis of Las17-GFP dynamics on the PM in living cells. The single frame was taken during bright-field (BF) and GFP fluorescence single-color imaging. A kymograph representation of Las17-GFP in live-cell movies (1 frame per second) in WT cells (*Upper*) and *bzz1Δ* (*Lower*) mutants is shown. White dashed lines indicate the regions used for kymographs. (Scale bar: 2 μm.) (*G*) Tracking of two individual Las17-GFP patches from TIRF images. Positions of the centers of patches were determined in each frame of a movie (1 frame per second). Consecutive positions from the start (green) to the end (red) are connected by lines. (Scale bar: 100 nm.) (*H*) Histogram shows the distribution of distances between appearance and disappearance sites for Las17-GFP imaged using TIRF microscopy. (*I*) Kymograph representation from TIRF imaging of Las17-GFP sliding along the PM in *rvs167Δ*, *bzz1Δ rvs167Δ*, *rvs167Δ bbc1Δ*, and *bzz1Δ rvs167Δ bbc1Δ* mutants from movies (1 frame per second). (*Left*) Images are the first frames of each movie. Kymographs were obtained from a single patch for each mutant. White dashed lines represent the PM. (Scale bar: 400 nm.) (*J*) Kymograph representations of Bzz1-GFP and Sla1-RFP of a single patch in an *rvs167Δ* mutant from a two-color movie of a medial focal plane in wide-field microscopy (1 frame per second). (Scale bar: 400 nm.)

different position (134 nm, $n = 45$ from 18 cells; Fig. 5*E*), implicating loss of F-BAR function in the retraction displacement phenotype.

To examine Bzz1's contribution to endocytic site stability during retraction in the presence of Bbc1, Las17-GFP dynamics were analyzed using total internal reflection fluorescence (TIRF) microscopy, which images the cell surface to a depth of only ~100 nm. Las17-GFP, which localizes to the base of endocytic invaginations and possibly along the tubule, did not move from its original position throughout its lifetime in WT cells (Fig. 5 *F* and *G* and Movie S7). In *bzz1Δ* mutant cells, however, Las17-GFP appeared and at first remained stationary but then moved on the membrane surface before disappearing (Fig. 5 *F* and *G* and Movie S7). We quantified the distance between appearance and disappearance positions from TIRF imaging of various mutants. As shown in Fig. 5*H*, in WT cells, Las17-GFP fluorescence centroids ended, on average, 73 nm ($n = 42$ from 19 cells) from the appearance position, but they ended 114 nm ($n = 50$ from 20 cells) from the appearance position in *bzz1*Δ mutants. The Las17-GFP patches also remained near their original position in *rvs167*Δ mutants (78 nm, $n = 48$ from 15 cells). In agreement with the results from single-mutant cells, Las17-GFP in *bzz1*Δ *rvs167*Δ mutant cells displayed movement as well (average = 116 nm, $n = 44$ from 18 cells). These results show that Bzz1 prevents sliding of endocytic invaginations along the plasma membrane. The timing of the movements and their occurrence in *bzz1*Δ single mutants, which do not show the retraction phenotype, are consistent with endocytic site movements occurring on initiation of actin polymerization and invagination formation.

We next determined whether internalization and retraction of Sla1, a marker for the invagination tip, occur coincident with the sliding of base-localized proteins along the plasma membrane in *bzz1*Δ *rvs167*Δ mutants. Two-color wide-field imaging demonstrated that Las17 stayed at the original position after Sla1-GFP internalization in an *rvs167*Δ mutant (Fig. S3*A*, *Left*). However, Las17-GFP patches slide away from their original position (Fig. 5*I*) in the direction of Sla1-RFP movement in *bzz1*Δ *rvs167*Δ mutants (Fig. S3*A*, *Right*), and the base began to move when Sla1 was internalized, suggesting that forces driving internalization are responsible for base sliding in *bzz1*Δ cells. The range of these movements was enhanced by *bbc1*Δ (Fig. S3*B*). To document movement of the invagination base further, we observed dynamics of the base-localized protein Myo5-GFP in both *rvs167*Δ and *bzz1*Δ *rvs167*Δ mutants. Just as with Las17-GFP patches, Myo5-GFP patches did not move from their origins in *rvs167*Δ mutants but slid together with Sla1-RFP patches in the *bzz1*Δ *rvs167*Δ mutant as Sla1-RFP internalized (Fig. S3*C*). These results establish a role for Bzz1 in stabilizing endocytic sites. Two-color imaging demonstrated that Bzz1 stays at the cortex after Sla1-GFP internalization in an *rvs167*Δ mutant (Fig. 5*J*), consistent with a role in maintaining stability of the membrane base during internalization and scission.

Ultrastructural Analysis Reveals that Rvs161/167 and Bzz1 Cooperate to Establish Proper Endocytic Membrane Geometry. Previously, yeast endocytic invaginations had been viewed ultrastructurally in chemically fixed cells and appeared as tubules of uniform diameter (4, 57). To gain insights into how Rvs161/167 and Bzz1 contribute to scission, we used a high-pressure freezing and freeze-substitution (HPF-FS) protocol to visualize endocytic site morphology in WT, *rvs167*Δ, *bzz1*Δ, and *bzz1*Δ *rvs167*Δ double-deletion strains (Fig. 6). Because furrow-like membrane compartment occupied by Can1 (MCC)/eisosome invaginations have been described in yeast EM studies (58–61), correct identification of endocytic invaginations is crucial. Importantly, because furrow invaginations are induced in stationary cells (58–61), we only analyzed log-phase cells. In our analysis, deep endocytic invaginations (>40 nm in length) in WT cells showed a flask-shaped morphology, with a wide base, narrow tubule, and wide bud (Fig. 6*A*, *Upper Left*). This flask shape is distinct from that of furrow invaginations, which have parallel membranes (61). Another distinctive feature of endocytic sites is a surrounding ribosome-free zone, which likely results from the actin cloud surrounding endocytic invaginations (4, 28, 57). These deep membrane invaginations are essentially identical to those established as endocytic sites by correlative fluorescence-transmission EM (28), and we confirmed by serial sectioning that they are tubular endocytic sites and not furrow-like MCC/eisosomes (Fig. S4). Moreover, we could observe these structures in small buds, which lack eisosomes (62).

In *rvs167*Δ cells, the diameter of the endocytic tubule was significantly larger relative to WT cells (6.6 ± 2.0-nm average tubule lumen diameter vs. 4.6 ± 2.1 nm in WT cells) (Fig. 6 *A*, *Lower Left*, and *B*), suggesting that Rvs proteins contribute to endocytic vesicle scission by constricting the tubule. Interestingly, cells lacking *BZZ1* show widened tubule regions (8.4 ± 2.7-nm tubule lumen diameter vs. 4.6 ± 2.1 nm in WT cells) (Fig. 6 *A*, *Upper Right*, and *B*) and the frequent occurrence (21%) of invaginations tilted from the perpendicular axis at angles beyond 30°, which was not observed in WT cells. Although the morphological changes in both single mutants were subtle, *rvs167*Δ *bzz1*Δ double-deletion cells showed a synergistic defect in tubule constriction, thus replacing flask-shaped invaginations by wide cylindrical invaginations (Fig. 6*A*, *Lower Right*) with both dra-

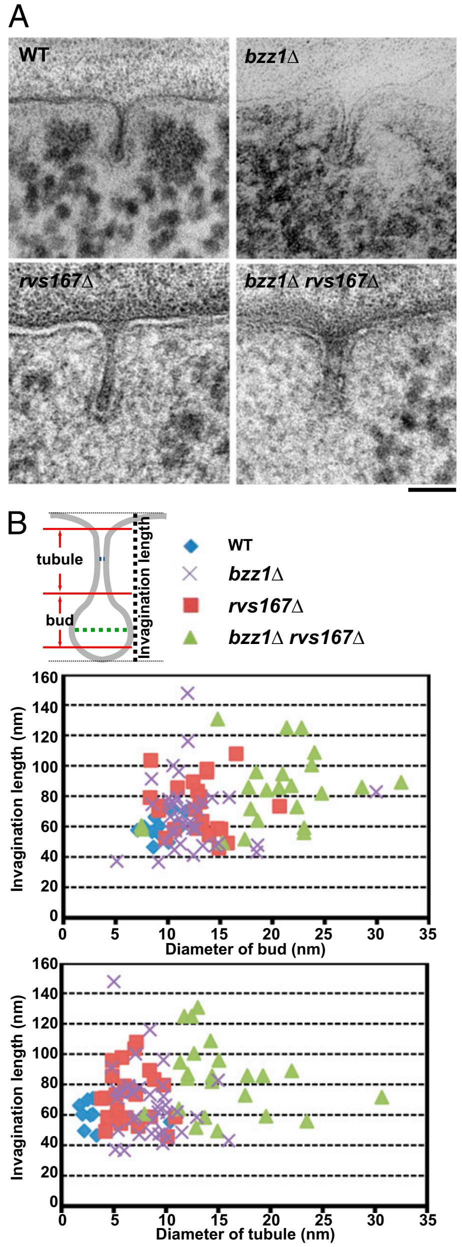

Fig. 6. Ultrastructural analysis of BAR and F-BAR domain protein roles in endocytic invagination geometry. (*A*) Deeply invaginated endocytic membranes (>40-nm length) were identified and measured. Representative electron micrographs of ultrathin sections demonstrating plasma membrane invaginations in WT cells and various mutants are shown. (Scale bar: 50 nm.) (*B*) Scheme used to measure the diameters of the endocytic membrane tubules and buds. Blue and green lines represent the positions used to measure tubule and bud diameters, respectively. Graphs represent tubule diameter (*Lower*) or bud diameter (*Upper*) vs. invagination length.

matically enlarged tubule (15.4 ± 5.0-nm tubule lumen diameter vs. 4.6 ± 2.1 nm in WT cells) and bud (20.2 ± 5.6-nm bud lumen diameter vs. 10.5 ± 2.1 nm in WT) diameters (Fig. 6*B*). Thus, the Bzz1 F-BAR protein cooperates with the Rvs161/167 BAR protein to establish proper invagination morphology. Furthermore, invaginations of 100 nm or more in length were more frequent in the *rvs167Δ* and *rvs167Δ bzz1Δ* deletion mutant strains, probably reflecting the membrane scission defect (Fig. 6*B*). The wide-neck phenotype, the *rvs167Δ bzz1Δ* double mutant, is completely distinct from any invagination seen in WT cells and is highly penetrant. None of the flask-shaped invaginations of WT cells can be found in *rvs167Δ bzz1Δ* double-mutant cells, and, conversely, there are no invaginations in WT cells that have the wide-neck phenotype.

Our EM studies lead us to conclude that formation of the characteristic flask shape of endocytic invaginations in budding yeast involves cooperation between the base formation activity of Bzz1 (F-BAR protein) and the tubule constriction activity of Rvs167 (BAR protein), augmented by actin assembly forces. Because tubules formed even in *rvs167Δ bzz1Δ* double mutants, we conclude that the primary function of the yeast Rvs161/167 BAR and Bzz1 F-BAR proteins in vivo lies in constriction and stabilization of the tubular endocytic membrane rather than in tubule formation.

Although BAR and F-BAR domains share some structural and biochemical features (63), several observations suggested that they have distinct functions in membrane remodeling. First, F-BAR domains generally form larger tubules (60–100 nm) than BAR domains (22-nm diameter) in vitro (13). The 22-nm value is similar to the yeast endocytic tubule's outer diameter of around 17 nm (~4.6 nm + 2 × 6-nm membrane bilayer width) that we measured for WT cells (Fig. 6 *A* and *B*). Second, F-BAR domains but not BAR domains are predicted to bind to flat membranes and to generate membrane curvature (64). Third, Bzz1-GFP (F-BAR domain) appears at endocytic sites about 10 s before Rvs167-GFP (BAR domain) in vivo (15). Fourth, Bzz1 localizes at the base of the endocytic invagination, whereas Rvs167 localizes along the length of the tubule region (which has a higher curvature) (this study and refs. 4, 5, 15). This last observation is consistent with spontaneous segregation of F-BAR and BAR proteins to adjacent membrane segments of the same tubules both in vivo and in vitro (64).

Synthesis. Integrating the various results presented here, we propose that Bzz1 F-BAR protein is recruited to endocytic sites when the membrane has a relatively low curvature and assembles a rigid invagination base (Fig. 7*A*, step 1). Bzz1 is a yeast homolog of metazoan syndapin and contains an N-terminal F-BAR domain and two SH3 domains implicated in actin assembly regulation at endocytic sites (15). Like BAR proteins, F-BAR proteins can induce membrane tubulation both in vivo and in vitro (9). In addition, many direct binding interactions between F-BAR and endocytic proteins have been discovered, and a role for F-BAR proteins in regulating actin polymerization in close proximity to the plasma membrane has been proposed (15, 54, 65).

Recently, the F-BAR protein FCHo, related to yeast Syp1, was shown by immuno-EM to associate with the bases of endocytic invaginations in mammalian cells (66). F-BAR domain proteins form ring- or spiral-like oligomers around the membrane tubules in vitro (13, 64). Such structures are predicted to be very rigid (64), and hence may provide a stable platform at the base of the invagination against which assembling actin filaments can generate forces. Interestingly, Bzz1 binds to the Arp2/3 activator Las17, and we propose that these proteins form a stable base, which resists actin assembly forces, enabling efficient actin assembly-driven endocytic tubule extension and constriction, which, in turn, generates higher membrane curvature (Fig. 7*A*, step 2). The BAR domain proteins are then recruited to these more highly curved membrane tubules, working cooperatively with actin assembly forces to create deeply invaginated endocytic membranes, resulting in further tubule constriction (Fig. 7*A*, step 3) and, ultimately, in scission (Fig. 7*A*, step 4). We speculate that in the absence of the F-BAR base, actin forces are not as coherently directed; as a result, the base moves in response to actin assembly forces and the invaginations tend to tilt to one side or the other (Fig. 7*B*).

A recent study of dynamin-deficient mammalian cells revealed striking similarities between endocytosis in mammals and yeast (7). Instead of the classic constricted clathrin-coated pits, dynamin-deficient mammalian cells formed long BAR protein-decorated tubules in an actin and BAR protein-dependent manner. These structures closely resemble yeast endocytic invaginations, whose formation is also mediated by actin and BAR protein assembly (Fig. 7*A*), providing strong support for the notion that actin and BAR proteins play similar roles during endocytosis in yeast and mammals.

Materials and Methods

Media and Strains. Yeast strains were grown in yeast-extract peptone dextrose (YPD) standard rich media or synthetic media supplemented with the appropriate amino acids. For induction of the *GAL1* promoter, 1.95% (wt/vol) galactose and 0.05% glucose were used as carbon sources. Yeast strains used in this study are listed in Table S2. Yeast strains carrying complete gene deletions or GFP or RFP tags were constructed by PCR-based procedures as described (67–69). Plasmids used in this study are listed in Table S3. Schemes detailing the construction of plasmids are available on request. Standard two-step PCR mutagenesis techniques were used for generation of plasmids for *BZZ1::HygMX* integration constructs, pDD2202. Integration of the correct allele was confirmed by sequencing.

Protein Purification and Actin Nucleation Assay. WT and mutant Bzz1 were overexpressed and purified by previously described procedures (37). Protein concentrations were determined using SYPRO dye (Molecular Probes) with purified rabbit actin as a standard. Actin nucleation assays were performed as described previously (15). Standard two-step PCR mutagenesis techniques were used for generation of the plasmid for protein purification, pDD2200.

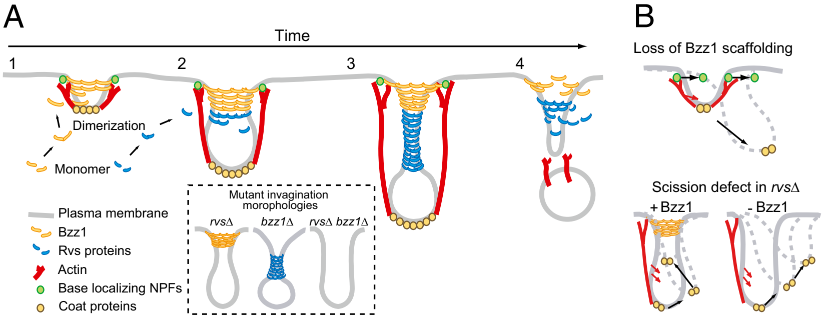

Fig. 7. Model for coordinated actions of BAR, F-BAR proteins, and actin assembly during invagination and scission (description is provided in the main text).

Microscopy. Images were acquired on a epifluorescence microscope (IX81; Olympus) equipped with a camera (Orca II; Hamamatsu Photonics) and a 1.4-N.A. objective lens and magnification of 100× as previously described (5). For TIRF imaging, the IX81 microscope equipped with a 1.65-N.A. objective lens and magnification of 100× and the expanded beam (488 nm) of an argon krypton laser (Melles Griot) were used. All image acquisition was performed using MetaMorph software (MDS Analytical Technologies). ImageJ (National Institutes of Health) was used for preparing kymographs and for general manipulation of images and movies. All imaging studies were performed at ∼25 °C in synthetic media. At least 100 patches from 10 cells were analyzed to quantify Sla1-GFP dynamics. The particle-tracking algorithm used for image analysis was described previously (27). Tracking of patches was performed from single-color GFP movies to achieve the best signal-to-noise ratio. TIRF images were obtained by previously described procedures (5). The LY uptake assay (70) and live-cell imaging (5) were performed as described previously. Tracking of α-factor was performed as described previously (71).

Retraction Phenotype Quantification. The retraction phenotype was scored visually by making kymographs for each patch using ImageJ. Patches were categorized into three classes of patch movement; internalization-scission, internalization-retraction, and no internalization. Patches that displayed internalization of less than one pixel were categorized as showing no internalization.

Liposome Preparation and Floating Assay. Chloroform solutions of phospholipids and derivatives, phosphatidylethanolamine (DOPE), phosphatidylcholine (DOPC), and PI(4,5)P$_2$, were purchased from Avanti Polar Lipids. Ergosterol was purchased from Sigma. SYPRO-Red protein stain was purchased from Molecular Probes. Liposomes were prepared, and liposome floating assays were performed as previously described (72). Bzz1, 0.6 μM, was incubated with liposomes in a 75-μL reaction. Liposome-associated proteins were resolved by SDS/PAGE and were stained with SYPRO dye. The liposome lipid composition was as follows: PC/PE: 53 mol% DOPC, 47 mol% DOPE; PC/PE with PI(4,5)P$_2$: 53 mol% DOPC, 42 mol% DOPE, 5 mol% PI(4,5)P$_2$.

Immunoprecipitation and Western Blotting. Immunoprecipitation was performed as described previously (73), with the following modifications. Cells were grown at 25 °C for 12 h to a cell density of 0.5 OD$_{600}$ per milliliter in YPD medium. Cells collected from a 150-mL culture were washed three times in cold water and resuspended in 0.6 mL of immunoprecipitation buffer [50 mM Tris·HCl (pH 7.5), 150 mM NaCl, 5 mM EDTA, 1% Nonidet P-40] containing protease inhibitor mixture set IV (purchased from Calbiochem). The cells were then lysed by agitation six times for 30 s with glass beads using a vortex mixer. Insoluble material was removed by centrifugation at ∼20,000 × *g* for 5 min at 4 °C. The cleared lysates were split into two aliquots; each was incubated with 3 μg of either anti-Myc antibody or control mouse IgG for 1 h at 4 °C. The samples were then rotated with 20 μL of protein G-Sepharose 4 Fast Flow (GE Healthcare Bio-Sciences) for 1 h at 4 °C. The beads were then pelleted and washed three times with immunoprecipitation buffer in the absence of detergents. The immunoprecipitated proteins were examined by Western blotting as described previously (73). The antibodies against myc and HA were generated in mouse and rabbit, respectively. Membranes were visualized by SuperSignal West pico-chemiluminescent substrate (Thermo Fischer Scientific).

Bioinformatics. Sequences were initially aligned using the CLUSTAL W program (DNA Data Bank of Japan), and the alignment was then optimized using the BOXSHADE program (Swiss Institute of Bioinformatics). The GenBank accession numbers for the sequences are as follows: *Homo sapiens* Formin-binding protein 17 FBP17 (Q96RU3.2), *H. sapiens* Cdc42-interacting protein 4 (Q15642.3), *Caenorhabditis elegans* (transducer of Cdc42-dependent actin assembly) homolog family member (toca-1) (NP_741722), *Rattus norvegicus* Syndapin 1 (Q9Z0W5.1), and *Saccharomyces cerevisiae* Bzz1 (P38822.1).

EM. Yeast cells were prepared by HPF-FS as described by Buser and McDonald (74), with modifications. Yeast cells were grown in YPD medium containing 1% glucose, collected by filtration through syringe filters (4-mm diameter), aspirated in cellulose capillaries (75), and high-pressure frozen in a Wohlwend HPF Compact 01 high-pressure freezer.

For structural studies of the membrane geometry, FS was carried out overnight in acetone containing 2% (vol/vol) glutaraldehyde, 0.1% uranyl acetate, and 5% (vol/vol) water (76, 77) using a Leica AFS FS system (Leica Microsystems). At room temperature, the samples were washed five times in ethanol and then infiltrated with 50% (vol/vol) Epon in ethanol for 2 h and pure Epon for 6 h. The Epon was exchanged once more and polymerized at 60 °C for 3 d. Thin sections (70 nm) were cut and collected on formvar-filmed copper grids and stained with 2% (wt/vol) aqueous uranyl acetate for 10 min and 2% (wt/vol) lead citrate for 1 min. The sections were observed at 120 kV in a Tecnai 12 transmission electron microscope (FEI) and recorded with an Ultrascan 1000 CCD camera (Gatan, Inc.). The resulting images were not software-processed except for brightness/contrast adjustments and image rotation.

ACKNOWLEDGMENTS. We are grateful to Dr. Georjana Barnes and the members of Drubin/Barnes laboratory for helpful discussions. The manuscript was improved by the critical comments of Voytek Okreglak, Helen Stimpson, and Jasper Weinberg. We thank Dr. Kazuma Tanaka for providing the pFA6a-HygMX vector and Dr. Kathryn Ayscough for yeast strains. This work was supported by National Institutes of Health Grants GM R01 42759 and GM R01 50399 (to D.G.D.). C.B. acknowledges a fellowship for prospective researchers from the Swiss National Science Foundation.

1. McMahon HT, Gallop JL (2005) Membrane curvature and mechanisms of dynamic cell membrane remodelling. *Nature* 438:590–596.
2. Liu J, Sun Y, Drubin DG, Oster GF (2009) The mechanochemistry of endocytosis. *PLoS Biol* 7:e1000204.
3. Stimpson HE, Toret CP, Cheng AT, Pauly BS, Drubin DG (2009) Early-arriving Syp1p and Ede1p function in endocytic site placement and formation in budding yeast. *Mol Biol Cell* 20:4640–4651.
4. Idrissi FZ, et al. (2008) Distinct acto/myosin-I structures associate with endocytic profiles at the plasma membrane. *J Cell Biol* 180:1219–1232.
5. Kaksonen M, Toret CP, Drubin DG (2005) A modular design for the clathrin- and actin-mediated endocytosis machinery. *Cell* 123:305–320.
6. Takei K, Slepnev VI, Haucke V, De Camilli P (1999) Functional partnership between amphiphysin and dynamin in clathrin-mediated endocytosis. *Nat Cell Biol* 1:33–39.
7. Ferguson SM, et al. (2009) Coordinated actions of actin and BAR proteins upstream of dynamin at endocytic clathrin-coated pits. *Dev Cell* 17:811–822.
8. Peter BJ, et al. (2004) BAR domains as sensors of membrane curvature: The amphiphysin BAR structure. *Science* 303:495–499.
9. Itoh T, et al. (2005) Dynamin and the actin cytoskeleton cooperatively regulate plasma membrane invagination by BAR and F-BAR proteins. *Dev Cell* 9:791–804.
10. Tsujita K, et al. (2006) Coordination between the actin cytoskeleton and membrane deformation by a novel membrane tubulation domain of PCH proteins is involved in endocytosis. *J Cell Biol* 172:269–279.
11. Dawson JC, Legg JA, Machesky LM (2006) Bar domain proteins: A role in tubulation, scission and actin assembly in clathrin-mediated endocytosis. *Trends Cell Biol* 16: 493–498.
12. Kessels MM, Qualmann B (2006) Syndapin oligomers interconnect the machineries for endocytic vesicle formation and actin polymerization. *J Biol Chem* 281:13285–13299.
13. Shimada A, et al. (2007) Curved EFC/F-BAR-domain dimers are joined end to end into a filament for membrane invagination in endocytosis. *Cell* 129:761–772.
14. Reider A, et al. (2009) Syp1 is a conserved endocytic adaptor that contains domains involved in cargo selection and membrane tubulation. *EMBO J* 28:3103–3116.
15. Sun Y, Martin AC, Drubin DG (2006) Endocytic internalization in budding yeast requires coordinated actin nucleation and myosin motor activity. *Dev Cell* 11:33–46.
16. Merrifield CJ, Perrais D, Zenisek D (2005) Coupling between clathrin-coated-pit invagination, cortactin recruitment, and membrane scission observed in live cells. *Cell* 121:593–606.
17. Doherty GJ, McMahon HT (2008) Mediation, modulation, and consequences of membrane-cytoskeleton interactions. *Annu Rev Biophys* 37:65–95.
18. Smythe E, Ayscough KR (2006) Actin regulation in endocytosis. *J Cell Sci* 119: 4589–4598.
19. Galletta BJ, Cooper JA (2009) Actin and endocytosis: Mechanisms and phylogeny. *Curr Opin Cell Biol* 21:20–27.
20. Yarar D, Waterman-Storer CM, Schmid SL (2005) A dynamic actin cytoskeleton functions at multiple stages of clathrin-mediated endocytosis. *Mol Biol Cell* 16: 964–975.
21. Saffarian S, Cocucci E, Kirchhausen T (2009) Distinct dynamics of endocytic clathrin-coated pits and coated plaques. *PLoS Biol* 7:e1000191.
22. Wu M, et al. (2010) Coupling between clathrin-dependent endocytic budding and F-BAR-dependent tubulation in a cell-free system. *Nat Cell Biol* 12:902–908.
23. Di Paolo G, et al. (2004) Impaired PtdIns(4,5)P2 synthesis in nerve terminals produces defects in synaptic vesicle trafficking. *Nature* 431:415–422.
24. Singer-Krüger B, Nemoto Y, Daniell L, Ferro-Novick S, De Camilli P (1998) Synaptojanin family members are implicated in endocytic membrane traffic in yeast. *J Cell Sci* 111:3347–3356.
25. Cremona O, et al. (1999) Essential role of phosphoinositide metabolism in synaptic vesicle recycling. *Cell* 99:179–188.
26. Sun Y, Carroll S, Kaksonen M, Toshima JY, Drubin DG (2007) PtdIns(4,5)P2 turnover is required for multiple stages during clathrin- and actin-dependent endocytic internalization. *J Cell Biol* 177:355–367.
27. Kaksonen M, Sun Y, Drubin DG (2003) A pathway for association of receptors, adaptors, and actin during endocytic internalization. *Cell* 115:475–487.
28. Kukulski W, et al. (2011) Correlated fluorescence and 3D electron microscopy with high sensitivity and spatial precision. *J Cell Biol* 192:111–119.

29. Smaczynska-de Rooij II, et al. (2010) A role for the dynamin-like protein Vps1 during endocytosis in yeast. *J Cell Sci* 123(Pt 20):3496–3506.
30. Okreglak V, Drubin DG (2007) Cofilin recruitment and function during actin-mediated endocytosis dictated by actin nucleotide state. *J Cell Biol* 178:1251–1264.
31. Galletta BJ, Chuang DY, Cooper JA (2008) Distinct roles for Arp2/3 regulators in actin assembly and endocytosis. *PLoS Biol* 6:e1.
32. Duncan MC, Cope MJ, Goode BL, Wendland B, Drubin DG (2001) Yeast Eps15-like endocytic protein, Pan1p, activates the Arp2/3 complex. *Nat Cell Biol* 3:687–690.
33. Toshima J, Toshima JY, Martin AC, Drubin DG (2005) Phosphoregulation of Arp2/3-dependent actin assembly during receptor-mediated endocytosis. *Nat Cell Biol* 7: 246–254.
34. Sirotkin V, Beltzner CC, Marchand JB, Pollard TD (2005) Interactions of WASp, myosin-I, and verprolin with Arp2/3 complex during actin patch assembly in fission yeast. *J Cell Biol* 170:637–648.
35. Evangelista M, et al. (2000) A role for myosin-I in actin assembly through interactions with Vrp1p, Bee1p, and the Arp2/3 complex. *J Cell Biol* 148:353–362.
36. Lechler T, Shevchenko A, Li R (2000) Direct involvement of yeast type I myosins in Cdc42-dependent actin polymerization. *J Cell Biol* 148:363–373.
37. Rodal AA, Manning AL, Goode BL, Drubin DG (2003) Negative regulation of yeast WASp by two SH3 domain-containing proteins. *Curr Biol* 13:1000–1008.
38. Soulard A, et al. (2002) Saccharomyces cerevisiae Bzz1p is implicated with type I myosins in actin patch polarization and is able to recruit actin-polymerizing machinery in vitro. *Mol Cell Biol* 22:7889–7906.
39. Giardini PA, Fletcher DA, Theriot JA (2003) Compression forces generated by actin comet tails on lipid vesicles. *Proc Natl Acad Sci USA* 100:6493–6498.
40. Collins A, Warrington A, Taylor KA, Svitkina T (2011) Structural organization of the actin cytoskeleton at sites of clathrin-mediated endocytosis. *Curr Biol* 21:1167–1175.
41. Liu AP, Fletcher DA (2006) Actin polymerization serves as a membrane domain switch in model lipid bilayers. *Biophys J* 91:4064–4070.
42. Saarikangas J, et al. (2009) Molecular mechanisms of membrane deformation by I-BAR domain proteins. *Curr Biol* 19:95–107.
43. Liu J, Kaksonen M, Drubin DG, Oster G (2006) Endocytic vesicle scission by lipid phase boundary forces. *Proc Natl Acad Sci USA* 103:10277–10282.
44. Römer W, et al. (2010) Actin dynamics drive membrane reorganization and scission in clathrin-independent endocytosis. *Cell* 140:540–553.
45. Roux A, et al. (2005) Role of curvature and phase transition in lipid sorting and fission of membrane tubules. *EMBO J* 24:1537–1545.
46. Baumgart T, Hess ST, Webb WW (2003) Imaging coexisting fluid domains in biomembrane models coupling curvature and line tension. *Nature* 425:821–824.
47. Rozovsky S, Kaizuka Y, Groves JT (2005) Formation and spatio-temporal evolution of periodic structures in lipid bilayers. *J Am Chem Soc* 127:36–37.
48. Veatch SL, Keller SL (2003) Separation of liquid phases in giant vesicles of ternary mixtures of phospholipids and cholesterol. *Biophys J* 85:3074–3083.
49. Lipowsky R (1992) Budding of membranes induced by intramembrane domains. *J Phys II France* 2:1825–1840.
50. Allain JM, Storm C, Roux A, Ben Amar M, Joanny JF (2004) Fission of a multiphase membrane tube. *Phys Rev Lett* 93:158104.
51. Stolz LE, Huynh CV, Thorner J, York JD (1998) Identification and characterization of an essential family of inositol polyphosphate 5-phosphatases (INP51, INP52 and INP53 gene products) in the yeast Saccharomyces cerevisiae. *Genetics* 148:1715–1729.
52. Stefan CJ, Padilla SM, Audhya A, Emr SD (2005) The phosphoinositide phosphatase Sjl2 is recruited to cortical actin patches in the control of vesicle formation and fission during endocytosis. *Mol Cell Biol* 25:2910–2923.
53. Toret CP, Lee L, Sekiya-Kawasaki M, Drubin DG (2008) Multiple pathways regulate endocytic coat disassembly in Saccharomyces cerevisiae for optimal downstream trafficking. *Traffic* 9:848–859.
54. Itoh T, Takenawa T (2009) Mechanisms of membrane deformation by lipid-binding domains. *Prog Lipid Res* 48:298–305.
55. Michelot A, et al. (2010) Reconstitution and protein composition analysis of endocytic actin patches. *Curr Biol* 20:1890–1899.
56. Costanzo M, et al. (2010) The genetic landscape of a cell. *Science* 327:425–431.
57. Mulholland J, et al. (1994) Ultrastructure of the yeast actin cytoskeleton and its association with the plasma membrane. *J Cell Biol* 125:381–391.
58. Moor H, Mühlethaler K (1963) FINE STRUCTURE IN FROZEN-ETCHED YEAST CELLS. *J Cell Biol* 17:609–628.
59. Takeo K, Shigeta M, Takagi Y (1976) Plasma membrane ultrastructural differences between the exponential and stationary phases of Saccharomyces cerevisiae as revealed by freeze-etching. *J Gen Microbiol* 97:323–329.
60. Walther P, Müller M, Schweingruber ME (1984) The ultrastructure of the cell surface and plasma membrane of exponential and stationary phase cells of Schizosaccharomyces pombe, grown in different media. *Arch Microbiol* 137:128–134.
61. Strádalová V, et al. (2009) Furrow-like invaginations of the yeast plasma membrane correspond to membrane compartment of Can1. *J Cell Sci* 122:2887–2894.
62. Moreira KE, Walther TC, Aguilar PS, Walter P (2009) Pil1 controls eisosome biogenesis. *Mol Biol Cell* 20:809–818.
63. Itoh T, De Camilli P (2006) BAR, F-BAR (EFC) and ENTH/ANTH domains in the regulation of membrane-cytosol interfaces and membrane curvature. *Biochim Biophys Acta* 1761:897–912.
64. Frost A, et al. (2008) Structural basis of membrane invagination by F-BAR domains. *Cell* 132:807–817.
65. Takano K, Toyooka K, Suetsugu S (2008) EFC/F-BAR proteins and the N-WASP-WIP complex induce membrane curvature-dependent actin polymerization. *EMBO J* 27: 2817–2828.
66. Henne WM, et al. (2010) FCHo proteins are nucleators of clathrin-mediated endocytosis. *Science* 328:1281–1284.
67. Longtine MS, et al. (1998) Additional modules for versatile and economical PCR-based gene deletion and modification in Saccharomyces cerevisiae. *Yeast* 14:953–961.
68. Goldstein AL, McCusker JH (1999) Three new dominant drug resistance cassettes for gene disruption in Saccharomyces cerevisiae. *Yeast* 15:1541–1553.
69. Kishimoto T, Yamamoto T, Tanaka K (2005) Defects in structural integrity of ergosterol and the Cdc50p-Drs2p putative phospholipid translocase cause accumulation of endocytic membranes, onto which actin patches are assembled in yeast. *Mol Biol Cell* 16:5592–5609.
70. Munn AL, Riezman H (1994) Endocytosis is required for the growth of vacuolar H(+)-ATPase-defective yeast: Identification of six new END genes. *J Cell Biol* 127: 373–386.
71. Toshima JY, et al. (2006) Spatial dynamics of receptor-mediated endocytic trafficking in budding yeast revealed by using fluorescent alpha-factor derivatives. *Proc Natl Acad Sci USA* 103:5793–5798.
72. Sun Y, Kaksonen M, Madden DT, Schekman R, Drubin DG (2005) Interaction of Sla2p's ANTH domain with PtdIns(4,5)P2 is important for actin-dependent endocytic internalization. *Mol Biol Cell* 16:717–730.
73. Saito K, et al. (2004) Cdc50p, a protein required for polarized growth, associates with the Drs2p P-type ATPase implicated in phospholipid translocation in Saccharomyces cerevisiae. *Mol Biol Cell* 15:3418–3432.
74. Buser C, McDonald K (2010) Correlative GFP-immunoelectron microscopy in yeast. *Methods Enzymol* 470:603–618.
75. Hohenberg H, Mannweiler K, Müller M (1994) High-pressure freezing of cell suspensions in cellulose capillary tubes. *J Microsc* 175:34–43.
76. Walther P, Ziegler A (2002) Freeze substitution of high-pressure frozen samples: The visibility of biological membranes is improved when the substitution medium contains water. *J Microsc* 208:3–10.
77. Buser C, Walther P (2008) Freeze-substitution: The addition of water to polar solvents enhances the retention of structure and acts at temperatures around −60 degrees C. *J Microsc* 230:268–277.